Infrared Physics & Technology 116 (2021) 103792

Contents lists available at ScienceDirect

Infrared Physics and Technology

journal homepage: www.elsevier.com/locate/infrared

Regular article

High-sensitivity refractive index sensor based on Ge–Sb–Se chalcogenide microring resonator

Wei Huang [a,d,f], Ye Luo [b,c], Wei Zhang [a,d,f,*], Chengdong Li [e], Lan Li [b,c], Zhen Yang [a,d,f], Peipeng Xu [a,d,f]

[a] Faculty of Electrical Engineering and Computer Science, Ningbo University, Ningbo 315211, China
[b] Key Laboratory of 3D Micro/Nano Fabrication and Characterization of Zhejiang Province, School of Engineering, Westlake University, 18 Shilongshan Road, Hangzhou 310024, China
[c] Institute of Advanced Technology, Westlake Institute for Advanced Study, 18 Shilongshan Road, Hangzhou 310024, China
[d] Key Laboratory of Photoelectric Detecting Materials and Devices of Zhejiang Province, Ningbo 315211, China
[e] Ningbo Institute of Oceanography, Ningbo University, Ningbo 315211, China
[f] Engineering Research Center for Advanced Infrared Photoelectric Materials and Devices of Zhejiang Province, Ningbo 315211, China

ARTICLE INFO

Keywords:
Chalcogenide glass
Microring resonator
Optical sening

ABSTRACT

In this article, we report a liquid sensing device based on a Ge–Sb–Se microring resonator (MRR) operating at a wavelength of 1550 nm. The transmission loss of the waveguide is 4.3 dB/cm, and the intrinsic *Q* factor of the MRR is 7.74×10^4, with an extinction ratio of approximately 40 dB. By detecting the different concentrations of NaCl solutions, we observe that the sensitivity of our proposed device is approximately 123 nm/RIU, and the intrinsic limit of detection is approximately 3.24×10^{-4} RIU. Compared with the other materials, such as silicon, Si_3N_4, or polymer, the moderate refractive index (RI) of $Ge_{28}Sb_{12}Se_{60}$ glass allows it to obtain a high sensitivity and a high *Q* factor, while maintaining a strong confinement on the light field to avoid suffering from bending loss under a small bending radius, with a compact structure.

1. Introduction

As an important part of information technology, sensing technology shoulders the important task of obtaining external information. Together with communication and computer technologies, they form the "senses", "nerve" and "brain" of information system, to jointly support the rapid development of the information society [1,2]. Among different types of sensors, optical sensor based on whispering gallery mode (WGM) provides low limit of detection (*LOD*) and high sensitivity, due to its high quality factor and small mode field volume [3–6]. To date, several types of WGM sensors with different structures have been reported, such as microrings, microdisks, microspheres, and microtoroids [7–9]. Among which, the WGM sensors based on microring resonator (MRR) have attracted much interest due to their high sensitivity to the change of external refractive index (RI) and the ability to work under single-mode condition [10–12]. As a optical resonant microcavity with compact structure, the light field can be confined to the order of micro-nano scale without using additional reflective mirrors. The cyclic resonance of the light field in such a small area can significantly enhance the interaction with external analyte, which will greatly improve the sensitivity and *LOD* of the sensor. Meanwhile, the fabrication of the microring is fully compatible with the CMOS semiconductor micro-nano manufacturing process, which is suitable to build a fully functional "lab on chip" system.

Many materials, such as lithium niobite [13], silicon nitride [14], III–V group semiconductors [15], polymers [16], and chalcogenide glasses (ChGs) [17–19], have been used to fabricate various photonic devices for sensing applications. ChGs are amorphous materials formed by covalent bonding of elements such as sulfur, selenium, and tellurium in Group VIA, with a certain amount of other metal or non-metal elements [20,21]. Compared with oxide counterparts, chalcogenides have higher glass density and contain atoms with high polarizability, which leads to higher linear and nonlinear RIs. In addition, because the atomic mass of chalcogenide elements (S, Se, Te) is heavier than that of oxygen, they have lower phonon energy (200–400 cm^{-1}), which makes the transparency window can be extended up to 12, 16 and 25 μm, for sulfides, selenides and tellurides respectively [22,23]. Such a wide infrared transparency window covers the characteristic absorption

* Corresponding author.
E-mail address: zhangwei3@nbu.edu.cn (W. Zhang).

https://doi.org/10.1016/j.infrared.2021.103792
Received 11 March 2021; Received in revised form 19 May 2021; Accepted 21 May 2021
Available online 28 May 2021
1350-4495/

bands for many biochemical molecules, which makes ChGs a very promising platform for infrared sensing applications.

Meanwhile, the RI of ChGs is higher than that of materials such as silicon nitride or polymers, which enables ultra-compact photonic devices without suffering from large bending losses. Furthermore, the amorphous property of ChGs enable us to efficiently deposit large-area and high-quality thin films on almost any substrate at a very low cost without considering lattice mismatch. Several ChG materials such as As_2S_3 [24], As_2Se_3 [25], and $Ge_{11.5}As_{24}Se_{64.5}$ glasses [26], have been used to make photonic devices for various sensing applications. However, the extreme harm of Arsenic to the natural environment and human beings will greatly limit their application. At this time, Arsenic-free and selenium-based ChGs provide an alternative option. Several studies have illustrated that the thermal and chemical stabilities of Ge-Sb-Se glasses are comparable to those of As-Se glasses, with a relatively large glass-formation region and excellent mid-infrared transparency [27,28]. Moreover, according to Miller's law, the third-order nonlinearity of selenium-based glass can be improved after replacing arsenic with antimony, because the stronger cationic polarizability of antimony [29,30]. Recently, these excellent properties of Ge-Sb-Se glasses have attracted interest in various fields, such as supercontinuum generation [31,32], wavelength conversion [33], all-optical signal processing, and sensing.

In this article, we report a compact $Ge_{28}Sb_{12}Se_{60}$ MRR sensor fabricated on a standard Si/SiO_2 platform. By adopting a microring structure with the resonance enhancement effect, the refractive index sensitivity as high as 123 nm/RIU is obtained through sensing in aqueous solutions with different NaCl concentrations. We prove that chalcogenide materials have a great application prospect not only in the mid-infrared wavelength range but also in the near-infrared wavelength range.

2. Microring resonator design

$Ge_{28}Sb_{12}Se_{60}$ glass is selected as core materials, and silicon wafers with a 2 μm thick layer of silicon dioxide are used as a buffer to design MRR devices. The thermally grown oxide layer helps prevent light leakage into the substrate due to the higher index contrast between the ChG and the silicon dioxide. Fig. 1(a) shows the schematic of the proposed sensor device, which consists of two bus waveguides and a ring resonator. Fig. 1(b) shows the cross-section view of the device, in which the waveguides and resonators have a height of 300 nm, and a vertical sidewall profile without losing generality is assumed. Fig. 1(c) shows the simulated n_{eff} of TE_0, TE_1, TE_2, TE_3, TM_0, TM_1, and TM_2 modes with different waveguide widths based on Finite-Difference Eigenmode (FDE) solver (MODE Solutions). The figure shows that the fundamental and first-order modes of TE/TM can be effectively supported when the width of the waveguide is greater than 1000 nm, but only the fundamental mode of TE/TM can be supported when the width of the waveguide is reduced below 750 nm. To avoid multiple modes, which may interfere with one another during propagation and will cause unwanted resonance peaks in the output spectrum, the width of the waveguide should be controlled below 750 nm. However, a very small size of the resonator will cause not only a high scattering loss due to the strong interaction between the light field and sidewall of the waveguide but also a challenge in device fabrication and characterization. Finally, the microring and the coupling waveguides are determined to have cross-sectional dimensions of 600 nm × 300 nm as a trade-off between the single-mode working condition, scattering loss, fabrication difficulty, and device robustness.

The fundamental mode profile for TE mode of the waveguide is shown in Fig. 2(a), in which the n_{eff} is calculated as approximately 2.002. By integrating the Poynting vector, about 80.386% of the power is confined in the waveguide core, and the effective area (A_{eff}) of the mode field is calculated to be 0.3 μm^2 using the following expression:

$$A_{eff} = \frac{\left(\iint |E(x,y)|^2 dxdy\right)^2}{\iint |E(x,y)|^4 dxdy}$$

where $E(x, y)$ is the transverse electric field of the mode. The cross-section profile of TE mode field distribution for the coupling area of the resonator is shown in Fig. 2(b), in which about 1.363% of the power is confined in the slot between the waveguide and the microring.

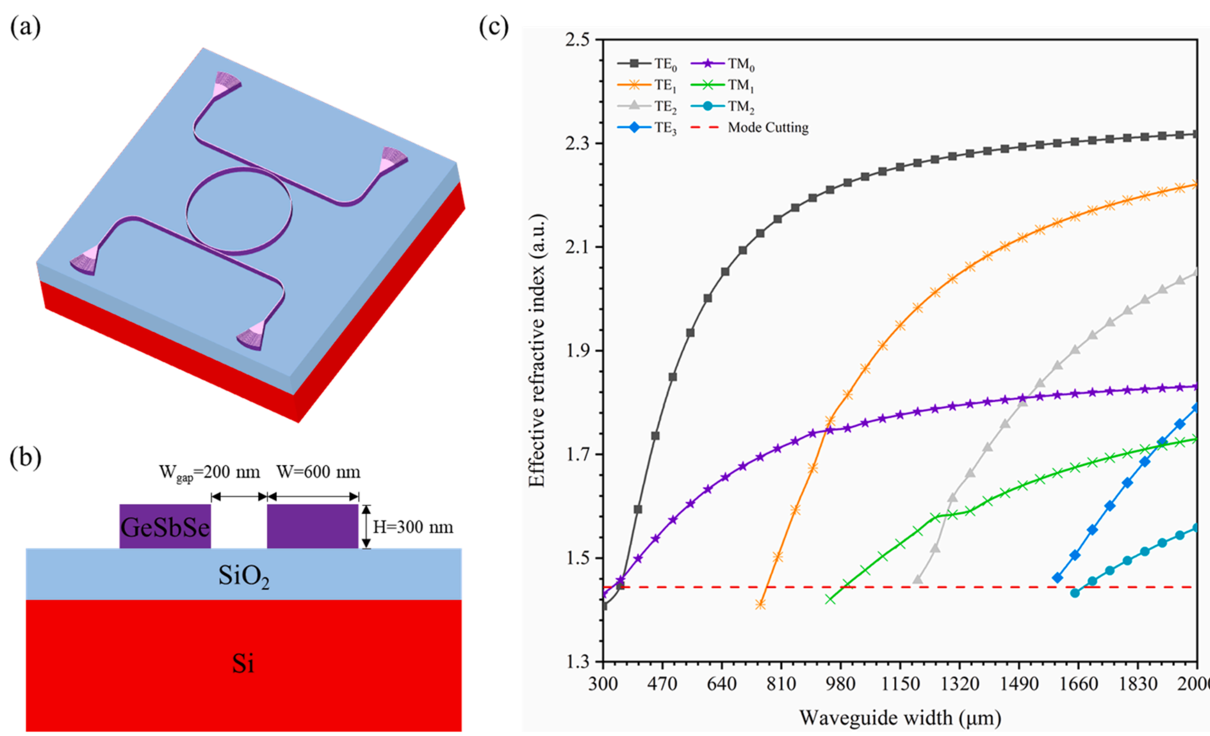

Fig. 1. Schematic configuration of the $Ge_{28}Sb_{12}Se_{60}$ sensor based on an add-drop MRR: (a) 3D view, (b) Cross-section view of the coupling region, (c) Effective RI of the different order of TE/TM modes with the waveguide width at 1550 nm wavelength.

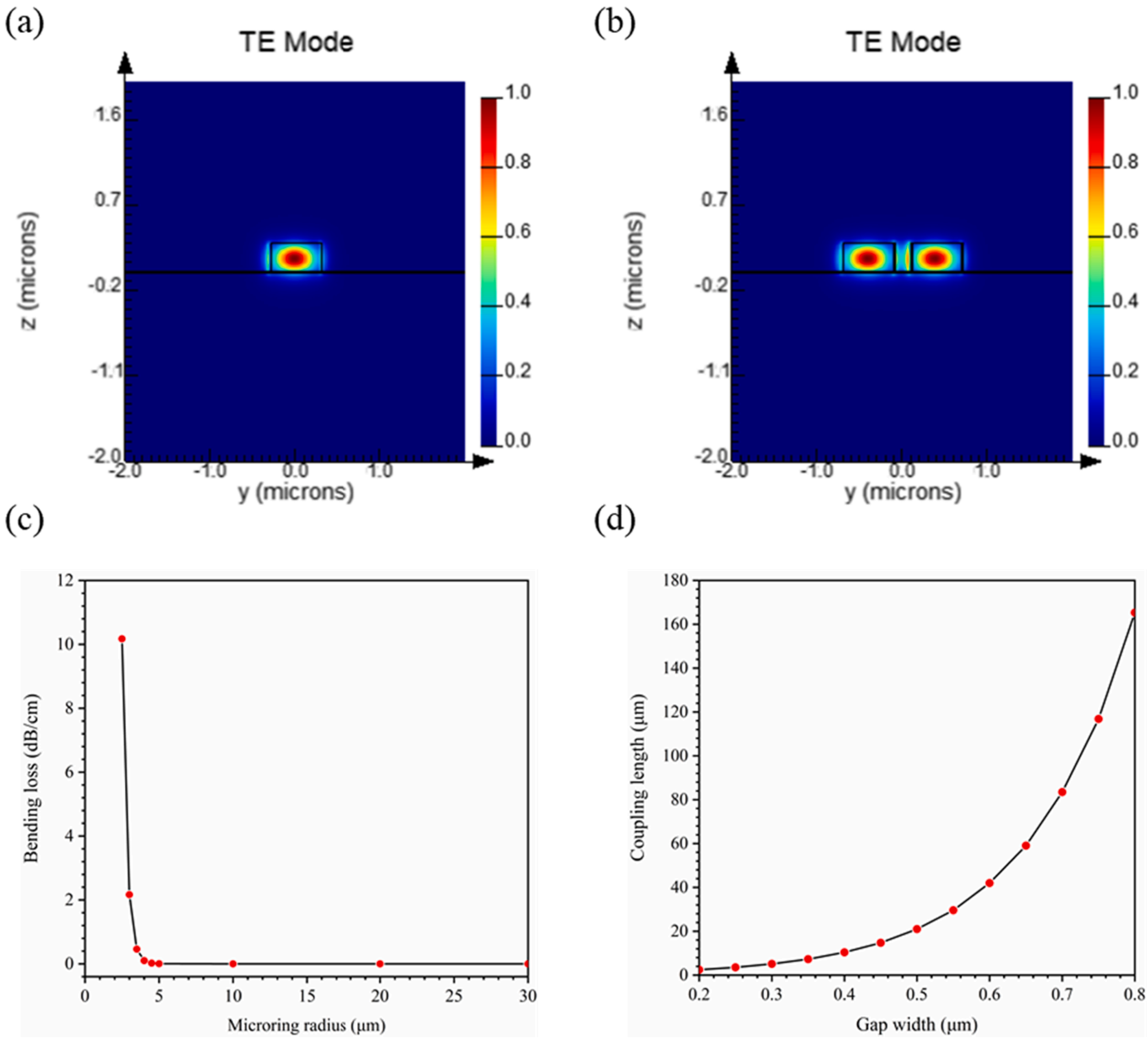

Fig. 2. Electric field distributions of (a) Fundamental TE mode in a 600 nm × 300 nm strip $Ge_{28}Sb_{12}Se_{60}$ waveguide with air upper cladding and SiO_2 substrate. (b) Cross-section field distribution of TE mode for the coupling area of the resonator. (c) Simulated bending loss variation as the radius of the microring resonator. (d) Simulated coupling length variation as the gap (the coupling coefficient is 0.01).

As mentioned before, the resonator is in a resonance state when the wavelength meets $2\pi Rn_{eff} = m\lambda$. A larger radius can increase the Q value of the sensor, thereby obtaining a lower detection limit. According to $FSR = \lambda^2/(n_g \times 2\pi R)$, a relatively small radius is needed to increase the sensing range. However, the bending loss will be increased sharply in a resonator with a very small radius. Fig. 2(c) illustrates the simulated results of the bending loss of a ring at different radii, where the bending loss is negligible when R is greater than 5 μm, and the radius of the Ge–Sb–Se MRR in our design is set as 24.6 μm. Fig. 2(d) also shows that when the power coupling coefficient is 0.01, coupling length will be increased by 50 times as the gap increases from 200 nm to 800 nm.

The transmission spectra of the designed MRR are also achieved based on 2.5D varFDTD solver (MODE Solutions). The transmission of the through and drop ports are shown in black and red lines in Fig. 3(a), respectively. The free spectrum range is calculated to be about 4.64 nm around the wavelength of 1550 nm from Fig. 3(b), which is in line with our design target. When the wavelength is far from the resonance wavelength as shown in Fig. 3(c), most of the energy is directly output from the through port of the micro ring, and a small part of the energy is coupled into the micro ring. When the wavelength satisfies the resonance condition as shown in Fig. 4(d), the energy is coupled from the bus waveguide, and resonance enhancement occurs in the ring and finally output from the drop port. In this case, the gap between the resonator and the waveguide is set as 200 nm to attain a near-critical coupling operation.

3. Microring resonator fabrication and characterization

The device fabrication begins with depositing a 300 nm thick $Ge_{28}Sb_{12}Se_{60}$ thin film by thermal evaporation on a 4-inch silicon wafer with a 2 μm thick silicon dioxide layer. A 300 nm thick negative electron beam resist (ma-N 2403) is then spin-coated onto the $Ge_{28}Sb_{12}Se_{60}$ film at a spinning speed of 4000 rpm. After being patterned by electron beam lithography (Raith Eline Plus) and developed in ma-D525 solution, an inductively coupled plasma (ICP) reactive ion etcher (Oxford Instruments plasma 100) was then used to etch the ChG core layer with a gas mixture of CF_4 and CHF_3, and the details of etching process could be found elsewhere [34]. When removing the residual photoresist, the device was first bombarded with the gas mixture of $CHF_3/AR/O_2$ for 20 s, then placed in 1-Methyl-2-pyrrolidone solution and shaken at 70 °C for 3 min. After being rinsed in deionized water and purged with nitrogen, it was finally dried on a hot plate at 110 °C for 10 min to

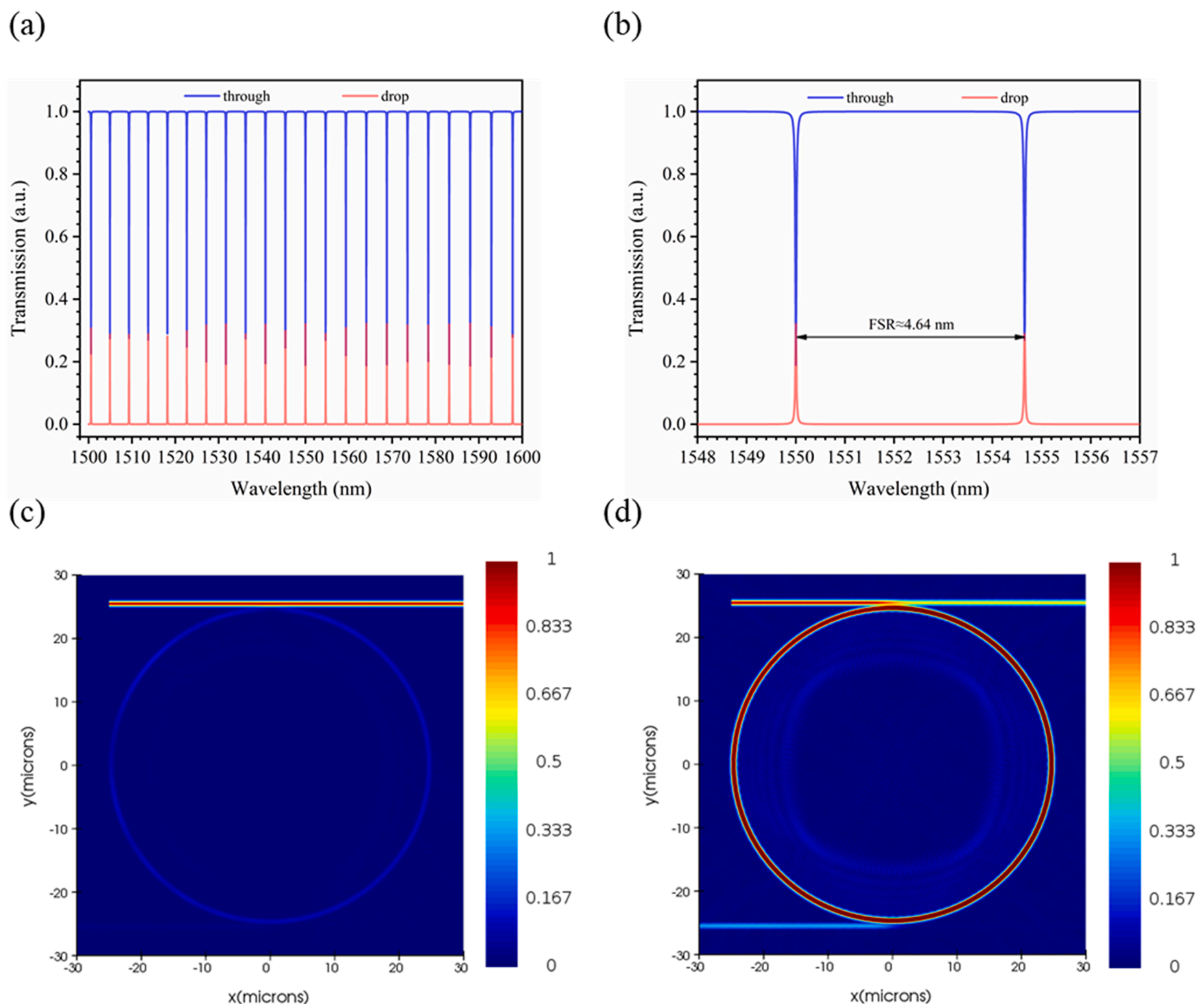

Fig. 3. (a) Transmission spectra of through port (black) and drop port (red) of the microring resonator at the wavelength of 1500–1600 nm. (b) Partially enlarged image of micro ring transmission. The electric field distribution of the microring resonator at a position (c) far from the resonance wavelength and (d) a resonant wavelength position.

completely remove surface moisture. Fig. 4(a) shows the schematic fabrication of the Ge–Sb–Se micro ring sensor. Fig. 4(b)–(d) show the scanning electron micrographs (SEMs) of the fabricated device, and Fig. 4 (e) shows a fully etched TE type focused subwavelength grating coupler, which is fabricated to facilitate the coupling of light from the fiber into and out of the waveguide, with a period of 920 nm and a duty cycle of 0.715.

The schematic diagram of the setup for device performance characterization is shown in Fig. 5(a). A continuous-wave semiconductor laser with a wavelength-tunable range from 1500 nm to 1630 nm is used as the light source, and a manual fiber polarization controller is used to adjust the polarization state of the output beam. A single-mode fiber with tapered end and a fully etched TE mode grating is used to couple light into the sample. Then a CCD camera is used to monitor the position of the single-mode fiber and the sample, and alignment can be reached by a 3-axis translation stage. Finally, the output optical signal is connected to a high-precision and sensitivity power meter through a single-mode optical fiber and recorded by a computer.

Fig. 5(b) shows a typical transmission spectrum measured from the drop port of the microring resonator. The resonance is fitted using the Lorentzian function to extract a 3 dB linewidth of $\delta\lambda = 0.04$ nm, as shown in Fig. 5(c). Using formula $Q = \lambda_0/\delta\lambda$, the load Q factor of the resonator is calculated to be slightly higher than 3.87×10^4, and the corresponding intrinsic Q factor can be estimated as 7.74×10^4 according to $Q_i = 2Q/(1+\sqrt{T_0})$,where T_0 is the transmission dip at resonance. Finally, propagation loss of the microring is calculated to be 4.3 dB/cm.

The transmission spectrum of the device measured in different concentrations of NaCl solution is shown in Fig. 5(d), and the enlarged view of red dot lines area in (d) is illustrated in Fig. 5(e). It is obvious that the resonance peaks are red-shift as the solution concentration increases. For the NaCl aqueous solution at 20 °C, the refractive index increases by about 0.0018 for 1% increase in the concentration [35]. In our experiment, the concentration of NaCl solution increased from 0% to 5% with a 1% step, and its corresponding refractive index increased from 1.333 to 1.342. In order to minimize the influence of external temperature fluctuations on the sensing experiment, a thermoelectric cooler is used to maintain the temperature of the sample stage at 20 °C. Meanwhile, after each test, the device will be rinsed in deionized water and placed on a 110 °C hot plate to completely dry it.

Sensitivity and *LOD* are two important indexes for evaluating sensor performance. *LOD* of a sensor depends not only on its own performance, but also on system noise, light sources, detectors, and data processing methods. When the noise is negligible, the intrinsic limit of detection (*iLOD*) is employed to replace the system's limit [36]: $iLOD = \lambda_{res}/(Q{\cdot}S)$, where λ_{res} is the sensor's resonant wavelength, and S is the

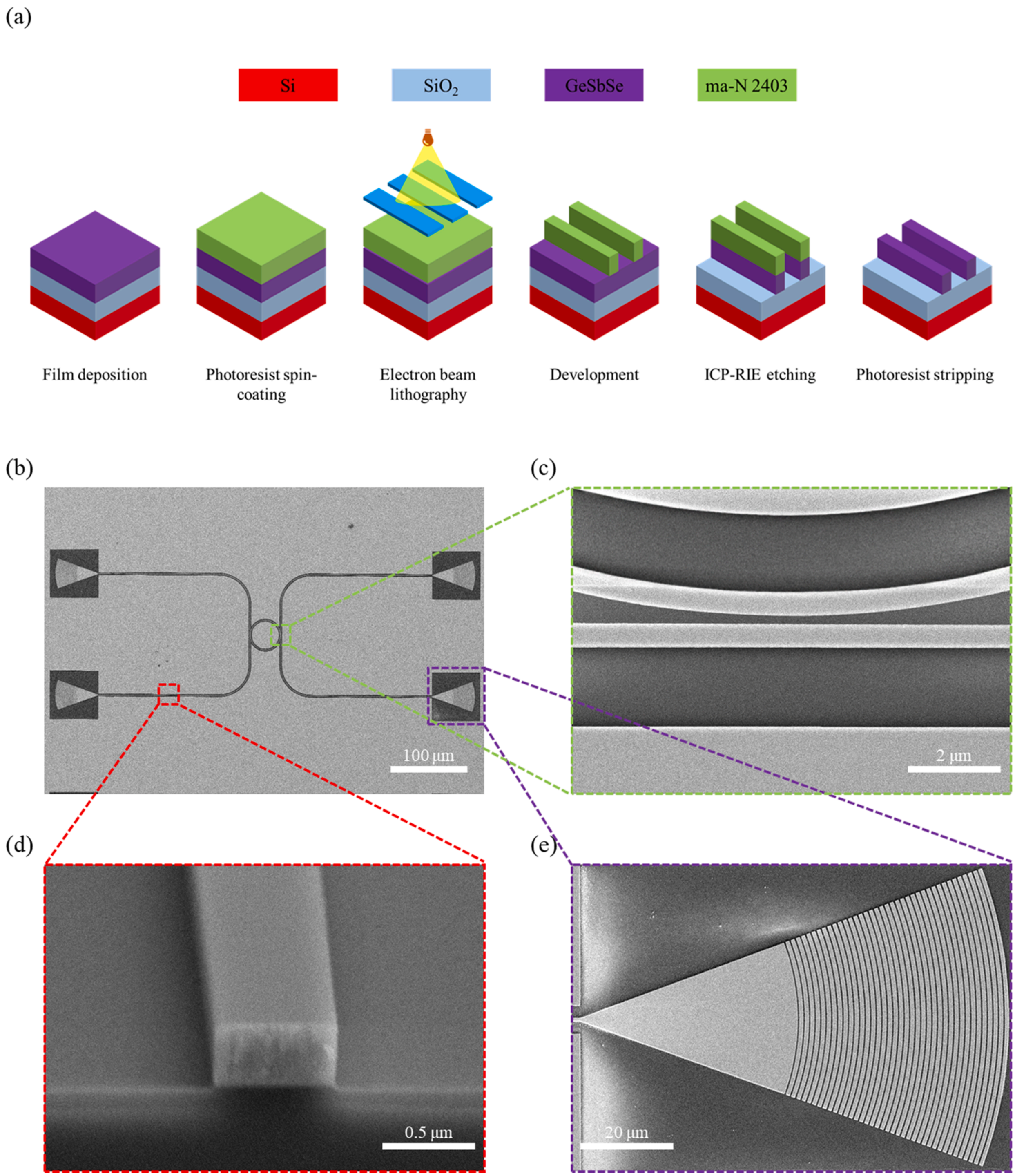

Fig. 4. (a) Schematic fabrication of Ge–Sb–Se micro ring sensor. (b) Top view of the entire device. (c) Enlarged view of the coupling region. (d) SEMs of the waveguide cross-section. (e) Fully etched TE type focused grating coupler.

sensitivity. After linear fitting, as shown in Fig. 5(f), the sensitivity S is determined to be approximately 123.68 nm/RIU and the corresponding *iLOD* is about 3.24×10^{-4} RIU.

A comparison between various photonic integrated RI sensors employing microring configuration in recent years is presented in Table 1 [37–48], which provides a perspective on the features and benefits of the proposed device. The optical field of the SOI platform-based micro ring is highly confined in the waveguide core and cannot fully interact with external analytes, which will result in low sensitivity usually around 60 nm/RIU. Subwavelength grating microring and photonic crystal microring resonators are proposed to improve the sensitivity of the sensor further. By periodically etching sub hundred nanometer cavities or slots on the micro ring, the light field can more fully interact with the external analyte, such that the sensitivity can be increased to near 400 nm/RIU. However, this will not only greatly increase the design and fabrication complexity but also increase the transmission loss of the waveguide to tens of dB/cm, substantially reducing the Q factor of the device to the order of 10^3. Several researchers have proposed to deposit a metal film on a dielectric to improve sensitivity by using the surface plasmon polariton effect at the

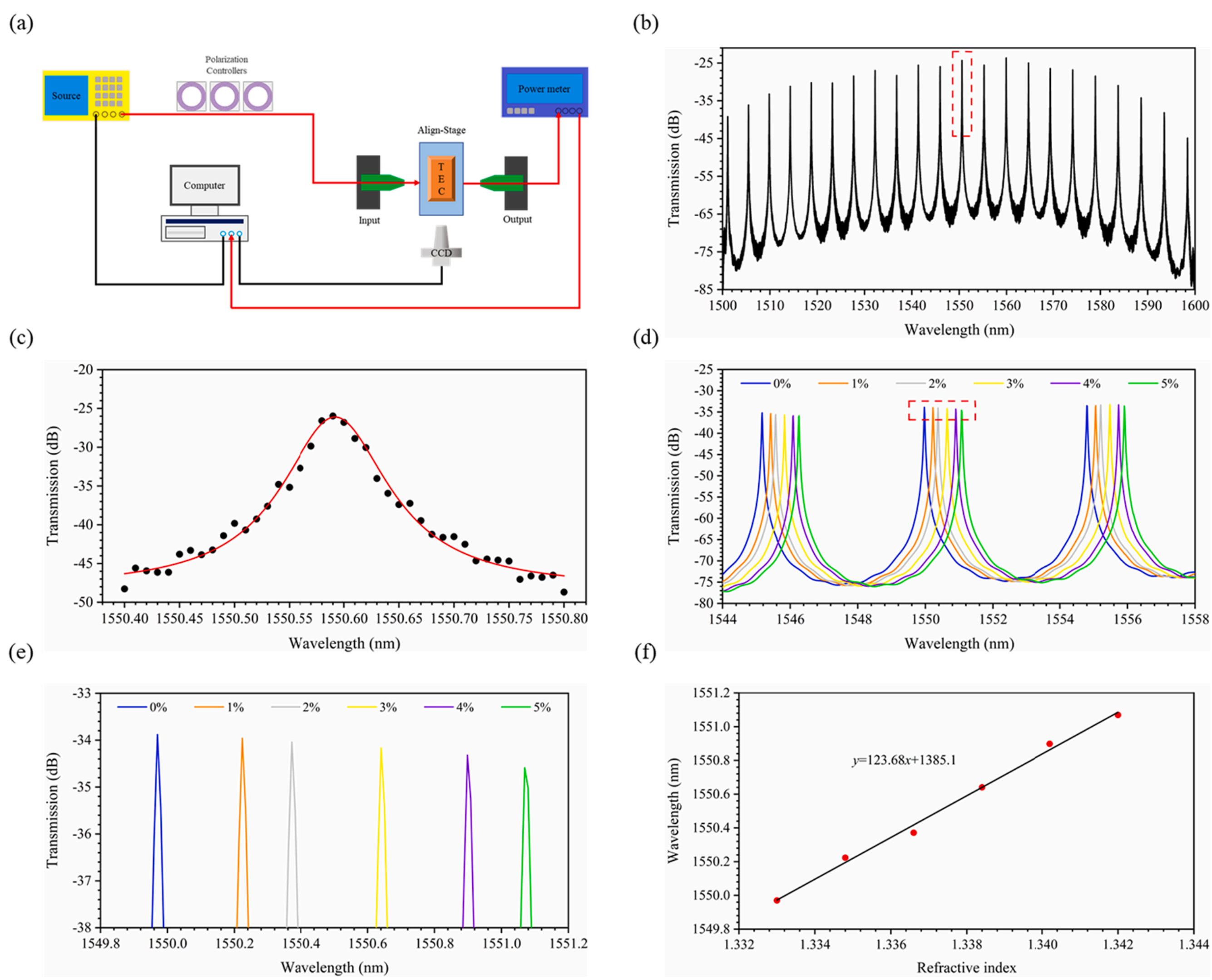

Fig. 5. (a) Schematic diagram of the experimental setup for transmission spectrum measurement. (b) The optical transmission spectrum of $Ge_{28}Sb_{12}Se_{60}$ MRR of the TE mode at drop port. (c) Experimental data of spectrum (black points) and the Lorentz fitting (red solid line) of one resonant peak. (d) Measured transmission responses of MRR immersed in aqueous NaCl solution with different concentrations. (e) The enlarged view of red dot area in (d). (f) Resonant wavelength of microring sensor as a function of background RI. The sensitivity of the microring sensor is 123.68 nm/RIU by the linear fitting.

Table 1
Comparison of the proposed microring sensor and other reported microring sensors.

Year	Material	Type	Radius (μm)	Q-factor	ER (dB)	Sensitivity (nm/RIU)	Exp or Sim
2014 [37]	SOI	Add-drop microring	5	1.5×10^5	16	65	simulation
2015 [38]	Si_3N_4	Differential microring	70	1.9×10^5	none	64.2	experiment
2015 [39]	Silicon + Silver	Hybrid plasmonic microring	5	6.0×10^2	none	497	simulation
2016 [40]	SiON	Racetrack microring	100	1.3×10^5	9	80	experiment
2017 [41]	SOI	Concentric dual-microring	5.5	none	30	180	simulation
2017 [42]	SOI	Photonic crystal microring	7.16	1.2×10^3	10	248	experiment
2017 [43]	SOI	Subwavelength grating microring	10	9.8×10^3	24.6	429.7	experiment
2018 [44]	SOI	Asymmetrical microring	1.7	1.7×10^3	none	80	simulation
2018 [45]	Si_3N_4	All-pass microring	none	$5.0 \times 10^3 \sim 8.0 \times 10^3$	~8	72.5	experiment
2018 [46]	SOI	Phase-shifted Bragg grating microring	3.5	2.0×10^3	20	297.13	simulation
2019 [47]	SOI	Subwavelength grating microring	10	3.5×10^4	none	672.8	simulation
2019 [48]	Al_2O_3	All-pass microring	200	6.0×10^5	none	102.3	experiment
This work	$Ge_{28}Sb_{12}Se_{60}$	Add-drop microring	24.6	7.7×10^4	~40	123.68	experiment

interface of the two materials, but this solution encounters the same problem due to the inherent high absorption of metals. Other researchers have focused on materials with lower RI than silicon, such as Si_3N_4, SiON, Al_2O_3, and polymers. The decrease in RI means that the confinement of the optical field in the waveguide core materials is weakened, such that the interaction between the optical field and the substance is strengthened to improve the sensitivity. But these micro rings need a much larger radius to avoid suffering from bending loss, which will be less compact for the structure of the device. Compared with the materials mentioned above, the moderate RI of $Ge_{28}Sb_{12}Se_{60}$

ChG allows it to obtain an increase in sensitivity (compared with silicon) while maintaining a stronger confinement on the light field (compared with Al_2O_3, polymer, and Si_3N_4) to avoid suffering from bending loss under a small bending radius, which will facilitate large-scale on-chip integration with other photonic devices.

4. Conclusion

In this article, a compact, fabrication-friendly liquid sensor based on $Ge_{28}Sb_{12}Se_{60}$ MRR is proposed. First, the single-mode transmission conditions of the $Ge_{28}Sb_{12}Se_{60}$ waveguide are investigated at 1550 nm wavelength to determine the geometrical dimensions. Then, the TE mode profile of the waveguide and coupling region as well as the bending loss under different radii and coupling length under different gap widths are simulated. Finally, the sensor is fabricated based on electron beam lithography and tested under a CW tunable laser and a high-resolution power meter to obtain intrinsic Q factors up to 7.74×10^4. Device size could be reduced to the order of tens of microns without suffering from substantial bending loss due to the high RI contrast between the ChG core layer and SiO_2 substrate. Considering the relatively lower RI of $Ge_{28}Sb_{12}Se_{60}$ ChGs compared with silicon, a higher sensitivity is expected, and 123.68 nm/RIU is experimentally demonstrated, with an *iLOD* of 3.24×10^{-4}. Our research suggests that $Ge_{28}Sb_{12}Se_{60}$ chalcogenide materials have a great application prospect in sensing fields with high sensitivity.

Funding

This work was supported by the Natural Science Foundation of Zhejiang Province (No. LD19F050001, No. LGJ18F050001, No. LY18F050005); by the National Key Research and Development Program of China (No. 2019YFB2203003); by the National Natural Science Foundation of China (No. 61875099); by the Natural Science Foundation of Ningbo (No. 202003N4007); and by the K. C. Wong Magna Fund at Ningbo University.

Declaration of Competing Interest

The authors declare that they have no known competing financial interests or personal relationships that could have appeared to influence the work reported in this paper.

References

[1] K.D. Heylman, K.A. Knapper, E.H. Horak, M.T. Rea, S.K. Vanga, R.H. Goldsmith, Optical Microresonators for Sensing and Transduction: A Materials Perspective, Adv. Mater. 29 (2017) 1700037.
[2] Y. Xu, P. Bai, X. Zhou, Y. Akimov, C.E. Png, L.-K. Ang, W. Knoll, L. Wu, Optical Refractive Index Sensors with Plasmonic and Photonic Structures: Promising and Inconvenient Truth, Adv. Opt. Mater. 7 (2019) 1801433.
[3] J. Zhou, J. Zheng, Z. Fang, P. Xu, A. Majumdar, Ultra-low mode volume on-substrate silicon nanobeam cavity, Opt. Express 27 (2019) 30692–30699.
[4] M.R. Foreman, J.D. Swaim, F. Vollmer, Whispering gallery mode sensors, Adv. Opt. Photon. 7 (2015) 168–240.
[5] X. Jiang, A.J. Qavi, S.H. Huang, L. Yang, Whispering-Gallery Sensors, Matter 3 (2020) 371–392.
[6] L. Cai, J. Pan, Y. Zhao, J. Wang, S. Xiao, Whispering Gallery Mode Optical Microresonators: Structures and Sensing Applications, Phys. Stat. Sol. (a). 217 (2020) 2070022.
[7] Y. Chen, J. Liu, Z. Yang, J.S. Wilkinson, X. Zhou, Optical biosensors based on refractometric sensing schemes: A review, Biosens. Bioelectron. 144 (2019) 111693.
[8] J. Wang, M.M. Sanchez, Y. Yin, R. Herzer, L. Ma, O.G. Schmidt, Silicon-Based Integrated Label-Free Optofluidic Biosensors: Latest Advances and Roadmap, Adv. Mater. Technol. 5 (2020) 1901138.
[9] S. Berneschi, F. Bettazzi, A. Giannetti, F. Baldini, G. Nunzi Conti, S. Pelli, I. Palchetti, Optical whispering gallery mode resonators for label-free detection of water contaminants, TrAC-Trend Anal. Chem. 126 (2020) 115856.
[10] W. Bogaerts, P. De Heyn, T. Van Vaerenbergh, K. De Vos, S. Kumar Selvaraja, T. Claes, P. Dumon, P. Bienstman, D. Van Thourhout, R. Baets, Silicon microring resonators, Laser Photonics Rev. 6 (2012) 47–73.
[11] M.C. Estevez, M. Alvarez, L.M. Lechuga, Integrated optical devices for lab-on-a-chip biosensing applications, Laser Photonics Rev. 6 (2012) 463–487.
[12] S. Feng, T. Lei, H. Chen, H. Cai, X. Luo, A.W. Poon, Silicon photonics: from a microresonator perspective, Laser Photonics Rev. 6 (2012) 145–177.
[13] C. Gutiérrez-Martínez, J. Santos-Aguilar, J. Meza-Pérez, A. Morales-Díaz, Novel Electric Field Sensing Scheme Using Integrated Optics $LiNbO_3$ Unbalanced Mach-Zehnder Interferometers and Optical Delay-Modulation, J. Lightwave Technol. 35 (2017) 27–33.
[14] V. Zamora, P. Lützow, M. Weiland, D. Pergande, Investigation of cascaded SiN microring resonators at 1.3 μm and 1.5 μm, Opt. Express 21 (2013) 27550–27557.
[15] R. Wang, S. Sprengel, A. Vasiliev, G. Boehm, J.V. Campenhout, G. Lepage, P. Verheyen, R. Baets, M.-C. Amann, G. Roelkens, Widely tunable 2.3 μm III-V-on-silicon Vernier lasers for broadband spectroscopic sensing, Photon. Res. 6 (2018) 858–866.
[16] N. Bavili, T. Balkan, B. Morova, M. Eryürek, Y. Uysallı, S. Kaya, A. Kiraz, Highly sensitive optical sensor for hydrogen gas based on a polymer microcylinder ring resonator, Sens. Actuators B Chem. 310 (2020) 127806.
[17] S. Levy, M. Klebanov, A. Zadok, High-Q ring resonators directly written in As_2S_3 chalcogenide glass films, Photonics Res. 3 (2015) 63–67.
[18] P. Ma, D.-Y. Choi, Y. Yu, Z. Yang, K. Vu, T. Nguyen, A. Mitchell, B. Luther-Davies, S. Madden, High Q factor chalcogenide ring resonators for cavity-enhanced MIR spectroscopic sensing, Opt. Express 23 (2015) 19969–19979.
[19] Z. Chen, L. Wan, J. Song, J. Pan, Y. Zhu, Z. Yang, W. Liu, J. Li, S. Gao, Y.-S. Lin, B. Zhang, Z. Li, Optical, mechanical and thermal characterizations of suspended chalcogenide glass microdisk membrane, Opt. Express 27 (2019) 15918–15925.
[20] B.J. Eggleton, B. Luther-Davies, K. Richardson, Chalcogenide photonics, Nat. Photonics 5 (2011) 141–148.
[21] X. Gai, T. Han, A. Prasad, S. Madden, D.-Y. Choi, R. Wang, D. Bulla, B. Luther-Davies, Progress in optical waveguides fabricated from chalcogenide glasses, Opt. Express 18 (2010) 26635–26646.
[22] Q. Du, Z. Luo, H. Zhong, Y. Zhang, Y. Huang, T. Du, W. Zhang, T. Gu, J. Hu, Chip-scale broadband spectroscopic chemical sensing using an integrated supercontinuum source in a chalcogenide glass waveguide, Photonics Res. 6 (2018) 506–510.
[23] A. Gutierrez-Arroyo, E. Baudet, L. Bodiou, J. Lemaitre, I. Hardy, F. Faijan, B. Bureau, V. Nazabal, J. Charrier, Optical characterization at 7.7 μm of an integrated platform based on chalcogenide waveguides for sensing applications in the mid-infrared, Opt. Express 24 (2016) 23109–23117.
[24] J. Hu, N. Carlie, L. Petit, A. Agarwal, K. Richardson, L. Kimerling, Demonstration of chalcogenide glass racetrack microresonators, Opt. Lett. 33 (2008) 761–763.
[25] T. Jin, J. Zhou, H.-Y.G. Lin, P.T. Lin, Mid-Infrared Chalcogenide Waveguides for Real-Time and Nondestructive Volatile Organic Compound Detection, Anal. Chem. 91 (2019) 817–822.
[26] P. Ma, D.-Y. Choi, Y. Yu, X. Gai, Z. Yang, S. Debbarma, S. Madden, B. Luther-Davies, Low-loss chalcogenide waveguides for chemical sensing in the mid-infrared, Opt. Express 21 (2013) 29927–29937.
[27] S. Dai, F. Chen, Y. Xu, Z. Xu, X. Shen, T. Xu, R. Wang, W. Ji, Mid-infrared optical nonlinearities of chalcogenide glasses in Ge-Sb-Se ternary system, Opt. Express 23 (2015) 1300–1307.
[28] W. Zhang, S. Dai, X. Shen, Y. Chen, S. Zhao, C. Lin, L. Zhang, J. Bai, Rib and strip chalcogenide waveguides based on Ge–Sb–Se radio-frequency sputtered films, Mater. Lett. 98 (2013) 42–46.
[29] M. Grayson, M. Zohrabi, K. Bae, J. Zhu, J.T. Gopinath, W. Park, Enhancement of third-order nonlinearity of thermally evaporated GeSbSe waveguides through annealing, Opt. Express 27 (2019) 33606–33620.
[30] M.R. Krogstad, S. Ahn, W. Park, J.T. Gopinath, Nonlinear characterization of $Ge_{28}Sb_{12}Se_{60}$ bulk and waveguide devices, Opt. Express 23 (2015) 7870–7878.
[31] A. Medjouri, D. Abed, Mid-infrared broadband ultraflat-top supercontinuum generation in dispersion engineered Ge-Sb-Se chalcogenide photonic crystal fiber, Opt. Mater. 97 (2019) 109391.
[32] M.A. Khamis, R. Sevilla, K. Ennser, Design of W-Type Index Chalcogenide Fiber for Highly Coherent Mid-IR Supercontinuum Generation, J. Lightwave Technol. 36 (2018) 5388–5394.
[33] E. Delcourt, N. Jebali, L. Bodiou, M. Baillieul, E. Baudet, J. Lemaitre, V. Nazabal, Y. Dumeige, J. Charrier, Self-phase modulation and four-wave mixing in a chalcogenide ridge waveguide, Opt. Mater. Express 10 (2020) 1440–1450.
[34] J. Zhou, Q. Du, P. Xu, Y. Zhao, R. Lin, Y. Wu, P. Zhang, W. Zhang, X. Shen, Large Nonlinearity and Low Loss Ge-Sb-Se Glass Photonic Devices in Near-Infrared, IEEE J. Sel. Top. Quantum Electron. 24 (2018) 1–6.
[35] C.-Y. Tan, Y.-X. Huang, Dependence of Refractive Index on Concentration and Temperature in Electrolyte Solution, Polar Solution, Nonpolar Solution, and Protein Solution, J. Chem. Eng. Data 60 (2015) 2827–2833.
[36] P. Xu, J. Zheng, J. Zhou, Y. Chen, C. Zou, A. Majumdar, Multi-slot photonic crystal cavities for high-sensitivity refractive index sensing, Opt. Express 27 (2019) 3609–3616.
[37] C. Ciminelli, F. Dell'Olio, D. Conteduca, C.M. Campanella, M.N. Armenise, High performance SOI microring resonator for biochemical sensing, Opt. Laser Technol. 59 (2014) 60–67.
[38] D. Kim, P. Popescu, M. Harfouche, J. Sendowski, M.-E. Dimotsantou, R.C. Flagan, A. Yariv, On-chip integrated differential optical microring refractive index sensing platform based on a laminar flow scheme, Opt. Lett. 40 (2015) 4106–4109.
[39] M. Zhang, G. Wu, D. Chen, Silicon hybrid plasmonic microring resonator for sensing applications, Appl. Opt. 54 (2015) 7131–7134.
[40] A. Samusenko, D. Gandolfi, G. Pucker, T. Chalyan, R. Guider, M. Ghulinyan, L. Pavesi, A SiON Microring Resonator-Based Platform for Biosensing at 850 nm, J. Lightwave Technol. 34 (2016) 969–977.

[41] L. Sun, J. Yuan, T. Ma, X. Sang, B. Yan, K. Wang, C. Yu, Design and optimization of silicon concentric dual-microring resonators for refractive index sensing, Opt. Commun. 395 (2017) 212–216.
[42] S.M. Lo, S. Hu, G. Gaur, Y. Kostoulas, S.M. Weiss, P.M. Fauchet, Photonic crystal microring resonator for label-free biosensing, Opt. Express 25 (2017) 7046–7054.
[43] L. Huang, H. Yan, X. Xu, S. Chakravarty, N. Tang, H. Tian, R.T. Chen, Improving the detection limit for on-chip photonic sensors based on subwavelength grating racetrack resonators, Opt. Express 25 (2017) 10527–10535.
[44] P. Zhang, Y. Ding, Y. Wang, Asymmetrical microring resonator based on whispering gallery modes for the detection of glucose concentration, Optik 171 (2018) 642–647.
[45] S. Das, S.C. Samudrala, K.J. Lee, B.R. Wenner, J.W. Allen, M.S. Allen, R. Magnusson, M. Vasilyev, Investigation of Si_3N_4 Microring Resonator for Bio-Chemical Sensing Applications. Frontiers in Optics/Laser Science, OSA Technical Digest, 2018. JW3A.98.
[46] C.Y. Zhao, L. Zhang, C.M. Zhang, Compact SOI optimized slot microring coupled phase-shifted Bragg grating resonator for sensing, Opt. Commun. 414 (2018) 212–216.
[47] N. Wu, L. Xia, Side-mode suppressed filter based on anangular grating-subwavelength grating microring resonator with high flexibility in wavelength design, Appl. Opt. 58 (2019) 7174–7180.
[48] M.D. Goede, M. Dijkstra, R. Obregón, J. Ramón-Azcón, E. Martínez, L. Padilla, F. Mitjans, S.M. Garcia-Blanco, Al_2O_3 microring resonators for the detection of a cancer biomarker in undiluted urine, Opt. Express 27 (2019) 18508–18521.